


## Article

# Investigation of Natural Weak Interface Properties and Their Impact on Fracture Propagation in Shale Reservoirs

Qi Chen <sup>1,2</sup> , Zhiqiang Huang <sup>1,2,\*</sup>, Xingjie Ling <sup>1,2,\*</sup>, Pengju Xu <sup>1,2</sup>, Lanke Tu <sup>3</sup>, Wenjing Liao <sup>4</sup>, Jun Xie <sup>5</sup>, Meng Wang <sup>4</sup>, Yijing Chen <sup>4</sup> and Lingli Li <sup>4</sup>

<sup>1</sup> College of Petroleum Engineering, Yangtze University, Wuhan 430100, China; 2021720471@yangtzeu.edu.cn (Q.C.); 2022720424@yangtzeu.edu.cn (P.X.)

<sup>2</sup> National Engineering Research Center for Oil & Gas Drilling and Completion Technology, Yangtze University, Wuhan 430100, China

<sup>3</sup> School of New Energy and Materials, China University of Petroleum, Beijing 102249, China; 2021215902@student.cup.edu.cn

<sup>4</sup> Southern Sichuan Gas Mine, PetroChina Southwest Oil & Gas Field Company, Luzhou 646000, China; snliaowenjing@petrochina.com.cn (W.L.); wangmeng6262@petrochina.com.cn (M.W.); snchenyijing@petrochina.com.cn (Y.C.); lilingli@petrochina.com.cn (L.L.)

<sup>5</sup> Northeast Sichuan Operation Branch, PetroChina Southwest Oil & Gas Field Company, Chongqing 405499, China; xiejun008@petrochina.com.cn

\* Correspondence: huangzq@yangtzeu.edu.cn (Z.H.); 2021720479@yangtzeu.edu.cn (X.L.)

**Abstract:** Horizontal well multi-cluster fracturing technology is crucial for the economic development of fractured shale reservoirs. The abundance of natural fractures in shale reservoirs significantly influences the propagation path of hydraulic fractures and determines the formation of complex fracture networks. To investigate the impact of natural weak planes on the geometric parameters of fractures in shale reservoirs, we first conducted tests on the mechanical characteristics of core samples from outcropping shale in the Weiyuan area using the indoor three-point bending method and digital image correlation (DIC) technology, providing data validation for subsequent numerical models. Secondly, considering the interaction between hydraulic and natural weak planes in three-dimensional space, we established a three-dimensional numerical model for horizontal well fracturing to simulate the synchronous competition and expansion of fractures in multi-cluster fracturing. Based on this foundation, we analyzed the influence of formation parameters and engineering parameters on the formation patterns of complex fracture networks. The results indicate that the difference in in situ stress is a significant factor affecting the selection of fracture propagation paths. As the in situ stress difference increases, it becomes more challenging to open natural fractures, leading to a reduced probability of activation of natural weak interfaces. When the cohesive strength of natural fractures is smaller, they are more likely to open and capture hydraulic fractures, thereby increasing shear slip length and fracture network area. Each fracturing stage has an optimal perforation density combination, where a higher density of perforations leads to reduced perforation pressure drop and weaker ability to mitigate inter-cluster stress interference. To achieve a comprehensive and balanced development of multi-clusters, the inter-cluster stress interference can be alleviated by increasing the perforation pressure drop. For dense perforation clusters, higher injection rates and viscosity can be employed to ensure the uniform development of multiple perforation clusters. This study provides new insights into predicting the formation of complex fracture networks in shale reservoirs and offers valuable guidance for optimizing hydraulic fracturing designs.

**Keywords:** shale reservoirs; natural fracture; multi cluster fracturing; 3D geological model; fracturing propagation path



**Citation:** Chen, Q.; Huang, Z.; Ling, X.; Xu, P.; Tu, L.; Liao, W.; Xie, J.; Wang, M.; Chen, Y.; Li, L. Investigation of Natural Weak Interface Properties and Their Impact on Fracture Propagation in Shale Reservoirs. *Processes* **2023**, *11*, 2697. <https://doi.org/10.3390/pr11092697>

Academic Editors: Hadi Jabbari, Vamegh Rasouli and Qingbang Meng

Received: 3 August 2023

Revised: 2 September 2023

Accepted: 7 September 2023

Published: 8 September 2023



**Copyright:** © 2023 by the authors. Licensee MDPI, Basel, Switzerland. This article is an open access article distributed under the terms and conditions of the Creative Commons Attribution (CC BY) license (<https://creativecommons.org/licenses/by/4.0/>).

## 1. Introduction

Currently, the global shale gas reserves amount to  $4.5624 \times 10^{14}$  m<sup>3</sup>, primarily distributed in North America, China, the Middle East, North Africa, and the former Soviet

Union. China possesses abundant shale gas resources, with preliminary estimates reaching  $(1.5\text{--}3.0) \times 10^{13} \text{ m}^3$ , placing it at the forefront worldwide [1,2]. In the economic development of shale gas reservoirs, the technology of multi-cluster hydraulic fracturing in horizontal wells plays a crucial role. Its technical characteristics are paramount for achieving optimal production rates in efficient oil and gas resource development [3]. Microseismic monitoring techniques indicate that the complex network of fractures formed during the process of multi-cluster hydraulic fracturing in horizontal wells determines the enhanced reservoir volume and influences the recovery factor of the target reservoir [4,5]. Natural fissures, as typical features of shale reservoirs, significantly impact the propagation path of hydraulic fractures, thereby governing the formation of the intricate fracture network. Therefore, it is imperative to investigate the mechanisms behind the formation of complex fracture networks during the volumetric fracturing of shale reservoirs induced by natural fissures.

Scholars both domestically and internationally have conducted numerous studies on the intersection and propagation of hydraulic fractures and natural fractures through physical laboratory experiments and numerical simulations. It is widely acknowledged that three scenarios exist when hydraulic fractures intersect with natural fractures: hydraulic fractures penetrate natural fractures, natural fractures divert hydraulic fractures, and hydraulic fractures follow the path of natural fractures [6]. Zhou et al. explored the macroscopic and microscopic influencing factors of hydraulic fracture propagation after interference with natural fractures using a large-scale true triaxial experimental system. They investigated the effects of natural fractures and in situ stress on hydraulic fracture propagation and fracture morphology [7]. Blanton et al. conducted extensive experiments on natural fracture-bearing sedimentary rocks and mudstone formations, revealing the influence of the inclination angle of natural fractures and stress difference on hydraulic fracture propagation [8]. Due to the limitations of theoretical and experimental research, many researchers have developed various numerical methods to simulate the interaction between hydraulic fractures and natural fractures. Zou et al. numerically studied the propagation of hydraulic fracture networks (HFNs) in natural fracture-bearing shale reservoirs based on a three-dimensional discrete element complex fracturing model, and validated the results through CT scanning technology [9].

Guo et al. utilized the cohesive finite element method to establish a two-dimensional model for the expansion of single-cluster fractures. They analyzed the influence of parameters such as the approach angle of hydraulic fractures, horizontal stress difference, viscosity, and displacement of fracturing fluid on the intersecting expansion patterns between hydraulic fractures and natural fractures. The results indicate that, in the absence of any criteria, the CZM model can effectively simulate the interaction between hydraulic fractures and natural fractures [10]. Gonzalez et al. employed four triangular cohesive elements to ensure the fluid continuity and pressure extension within the intersecting region of natural and hydraulic fractures. By utilizing the CZM method, they investigated the influence of the cohesive strength of natural fractures on the expansion behavior of hydraulic fractures [11]. De Pater and Nagel conducted a two-dimensional study using the DEM model to examine the expansion mechanism of fracture networks in fissured shale reservoirs in relation to the injection rate and viscosity of fracturing fluids [12,13].

Although the aforementioned studies address the interference of natural fractures on the formation of complex fracture networks, they fail to consider the impact of two mechanisms—stress shadow and flow distribution—on the competitive expansion of multiple fractures within a multi-cluster fracturing scenario. Moreover, most of these studies are limited to two-dimensional models. Zou et al., by employing CT scanning, provided a description of the geometric morphology of fractures in naturally fractured shale after hydraulic fracturing experiments. The results demonstrate that in three-dimensional space, the vertical stress difference tends to dominate the fracture morphology, and the height expansion of hydraulic fractures is influenced by the three-dimensional distribution of natural fractures [14]. Based on an analysis of the intrinsic mechanical mechanisms within fractures, researchers such as Roussel, Manchanda, and Wu argue that the mutual influence

among multiple fractures arises from the interference of stress shadows, which leads to the uneven development of these fractures [15–17]. Therefore, it is crucial to investigate the interaction between hydraulic fractures and natural fractures in a three-dimensional space within the context of multi-cluster fracturing.

This study focuses on fractured shale reservoirs in the Weiyuan region, taking X horizontal wells as an example. We employed indoor three-point bending (TPB) experiments in conjunction with digital image correlation (DIC) technology to measure the mechanical characteristic parameters of natural shale cores. Utilizing the coupled stress-permeability-damage cohesive zone method (CZM), we established a three-dimensional model that accounts for the competition and expansion of multiple hydraulic fractures in horizontal wells, considering the presence of natural fractures. Through this model, we investigated the interaction mechanisms between hydraulic fractures and natural weak planes, providing a quantitative representation of the expansion behavior of hydraulic fractures under the influence of geological and engineering parameters. This research provides new insights into predicting the formation of complex fracture networks in shale reservoirs and holds valuable references and guidance for optimizing hydraulic fracturing design.

## 2. Shale Mechanical Parameter Tests

### 2.1. Sampling and Processing of Natural Outcropping Shale

To verify the feasibility of this numerical approach and the accuracy of the simulation results, it is essential to conduct tests on the mechanical parameters of shale. For shale with developed natural weak planes, it is commonly regarded as a transversely isotropic material, where its strength, strain, fracture mechanisms, and fracture propagation patterns are closely related to the orientation of the natural weak planes. In addition to considering the orientation of natural weak planes, three typical relative positional relationships with pre-existing fracture openings should also be taken into account (Divider; Short-Transverse; and Arrester). Thus, following the collection of exposed shale samples in the Weiyuan region, the rock specimens were processed, with the dimensions of the core being length  $\times$  width  $\times$  height = 250  $\times$  50  $\times$  50 mm. Within the shale specimens, a pre-existing fracture was deliberately incorporated in the middle section, featuring an aperture height of 10 mm and a width of 2 mm (Figure 1a). Considering natural weak plane dip angles of  $\beta = 30^\circ$ ,  $60^\circ$ , and  $90^\circ$ , four specimens were prepared for each dip angle, resulting in a total of twelve shale specimens (Table 1). The specimens were subjected to a random speckle pattern using the technique of manual spray painting. A white paint layer was initially sprayed onto the surface of the shale specimens, and once it dried, a random speckle treatment was applied using black paint. During the process of creating the speckle pattern, meticulous attention was given to ensure a uniform distribution of black spots, thus achieving a high-contrast random grayscale distribution image (Figure 1b).

**Table 1.** Basic parameters of the model.

Dip Angle of Natural Weak Planes	Specimen No.	Size	Amount
30°	S30-1-1	250 $\times$ 50 $\times$ 50 mm	4
	S30-1-2	250 $\times$ 50 $\times$ 50 mm	
	S30-1-3	250 $\times$ 50 $\times$ 50 mm	
	S30-1-4	250 $\times$ 50 $\times$ 50 mm	
60°	S60-1-1	250 $\times$ 50 $\times$ 50 mm	4
	S60-1-2	250 $\times$ 50 $\times$ 50 mm	
	S60-1-3	250 $\times$ 50 $\times$ 50 mm	
	S60-1-4	250 $\times$ 50 $\times$ 50 mm	
90°	S90-1-1	250 $\times$ 50 $\times$ 50 mm	4
	S90-1-2	250 $\times$ 50 $\times$ 50 mm	
	S90-1-3	250 $\times$ 50 $\times$ 50 mm	
	S90-1-4	250 $\times$ 50 $\times$ 50 mm	

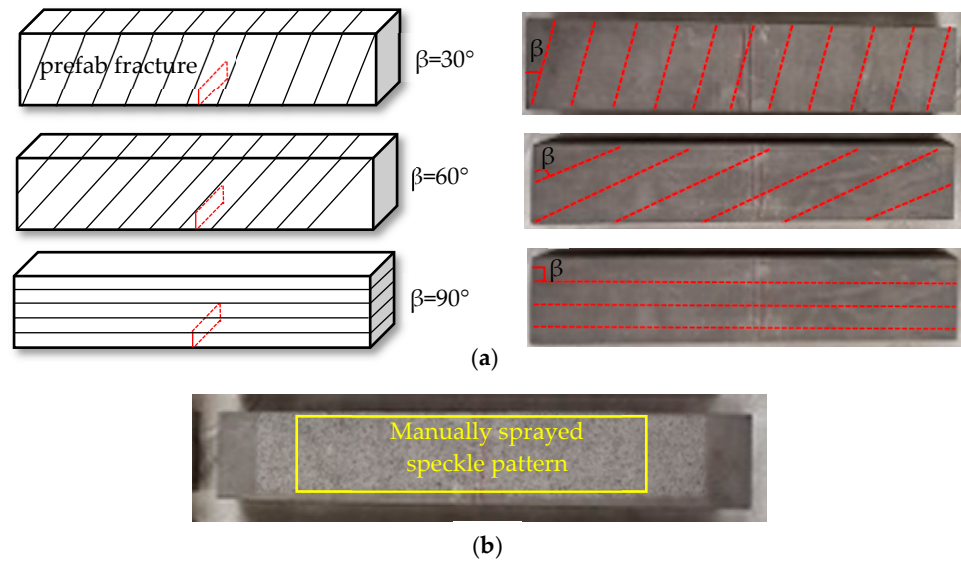


**Figure 1.** Preparation of natural outcropping shale samples: (a) Processed shale specimens; (b) artificially sprayed speckles on the shale surface.

## 2.2. Test Equipment

The natural shale outcrop artificial cores were subjected to three-point bending loading experiments using a universal material testing machine. The maximum experimental force of the testing machine was 200 kN, with a displacement resolution of 0.002 mm and a displacement rate adjustment range of 0.001 to 200 mm/min (Figure 2a,b). During the experiment, the setup can be considered as a simply supported beam under concentrated force, where  $P$  represents the load applied to the specimen,  $H$  is the specimen's height,  $B$  is the cross-sectional width of the specimen,  $S$  is the net span between the two supports, and  $L$  is the length of the sample, ensuring  $S/L = 0.85$  (Figure 2c). For simplicity in analysis, when the deformation is small, the displacement measured by the sensors is approximated as the deflection of the specimen. The data obtained from this experiment can be interpreted as the deflection of the specimen at the midpoint of its span under different applied loads  $P$ .

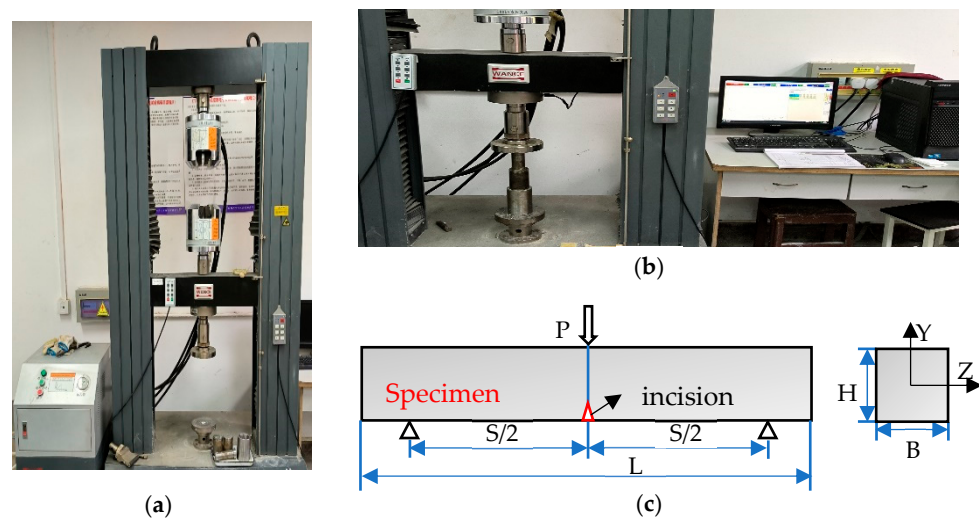


**Figure 2.** Three-point bending mechanical testing of shale: (a) universal material testing machine; (b) pressure control and data collection system; (c) Three-point bending test loading model.

A non-contact full-field deformation digital image correlation (DIC) optical measurement system was employed to capture the surface strain field of the specimen during three-point bending loading. The system primarily consists of an industrial CCD camera, artificial

point light source, and image data processing system. Throughout the experiment, the industrial camera digitally captured the speckle pattern on the surface of the artificially sprayed specimen, recording all digital images during the loading process and calculating the strain field during the specimen's failure. The underlying theory is based on analyzing the digital images of the surface before and after loading, matching corresponding geometric points in the images, relying on the invariant grayscale of the same point on the surface before and after deformation, and utilizing random speckles to ensure the uniqueness of any pixel subset in the image. The schematic diagram of the working principle is shown in Figure 3.

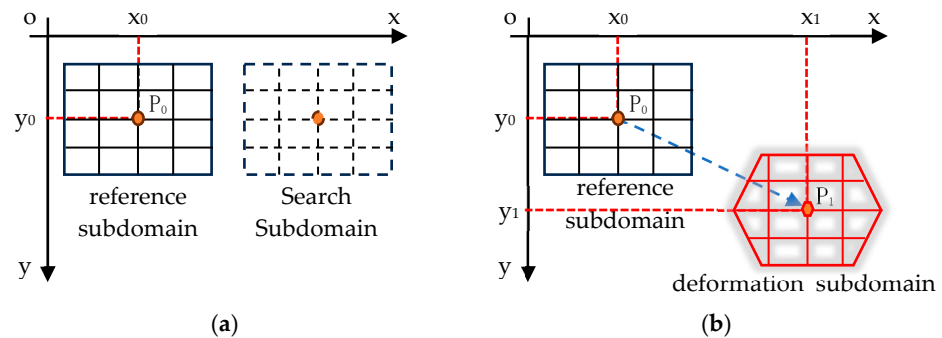


**Figure 3.** DIC optical measurement working principle diagram: (a) before specimen deformation; (b) after specimen deformation.

By comparing the two acquired images of the tested object's surface before and after deformation, surface displacements are determined through the probability-based statistical correlation of the randomly distributed speckle points. This process transforms deformation measurements into computable correlations, where the strain magnitude is obtained by subtracting the original coordinate values from the new coordinate values. Assuming that in the testing area, the pixel coordinates of points before and after deformation are denoted as  $P_0(x_0, y_0)$  and  $P_1(x_1, y_1)$ , respectively, their coordinate mapping relationship can be expressed as follows:

$$\begin{cases} x_1 = x_0 + u \\ y_1 = y_0 + v \end{cases} \quad (1)$$

where  $u, v$  are the translational displacements of the subdomain center points in the "x" and "y" directions.

Once the explicit mapping relationship is defined according to Equation (1), the similarity coefficient  $C(u, v)$  of the subdomains in the pre and post-deformation images is computed using the relevant formulas available in the computer. This coefficient serves as an assessment of the similarity between the subdomains before and after deformation. The computation of the functional relationship between the reference subdomain and the target deformed subdomain is carried out following the approach proposed in the reference.

$$C_{(u,v)} = \text{Coor}\{u(x_1, y_1), v(x_1, y_1)\} \quad (2)$$

where  $u(x_1, y_1)$  is the pixel coordinate grayscale of point  $P_0$  in the reference subdomain;  $v(x_1, y_1)$  is the pixel coordinate grayscale of the corresponding point  $P_0$  in the target deformed subdomain; and  $C(u, v)$  denotes the deformation function that describes the similarity between  $P_0$  and  $P_1$ .

### 2.3. Experiment Method

Figure 4 illustrates the entire testing system, comprising the three-point bending loading system, DIC optical measurement system, and strain testing system. Before the bending test, the CCD cameras are mounted on both sides of the specimen symmetrically, ensuring the acquisition of a complete analysis area on the surface of the specimen (in this study, the entire specimen region) for three-dimensional strain analysis. Finally, the camera lens aperture, focal

length, polarization, and the direction and position of the point light source are adjusted to achieve optimal shooting results. Once the experimental setup is complete, the specimen is placed on the three-point bending fixture with the side containing the speckle pattern images facing the CCD industrial camera of the DIC system. The universal material testing machine's load head is adjusted so that it just contacts the surface of the specimen, and the CCD recording is initiated simultaneously when loading begins. To simulate a quasi-static failure process, the bending test loading rate is set at 0.5 mm/min, the shutter speed is set at 1/5 s, and the load interval for image acquisition is 10 N.

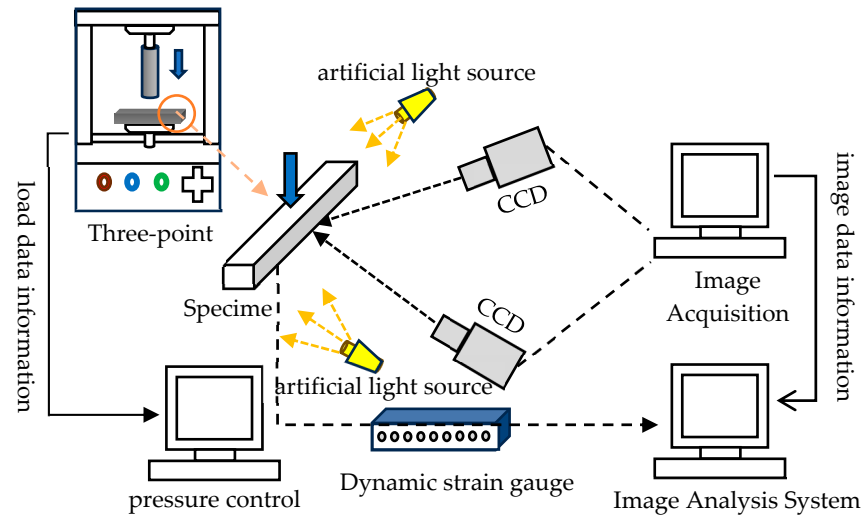


**Figure 4.** System for three-point bending fracture testing of shale specimens.

#### 2.4. Experiment Data Processing

By utilizing experimental data and relevant theoretical formulas, the mechanical anisotropic parameters of shale are calculated, specifically for the three-point bending case, as follows:

$$f\left(\frac{a}{H}\right) = \frac{3\frac{S}{H}\sqrt{\frac{a}{H}}}{2\left(1+2\frac{a}{H}\right)\left(1-\frac{a}{H}\right)^{3/2}} \times \left[1.99 - \frac{a}{H}\left(1-\frac{a}{H}\right)\left\{2.15 - 3.39\left(\frac{a}{H}\right)\right\} + 2.7\left(\frac{a}{H}\right)^2\right] \quad (3)$$

where  $S$ ,  $W$ , and  $H$  are the span, thickness and height of the specimen, mm; and  $a$  is the length of the prefabricated fracture, mm.

The equation for calculating the fracture toughness of shale specimens is as follows [18]:

$$K_{IC} = \frac{F_{max}}{W\sqrt{H}}f\left(\frac{a}{H}\right) \quad (4)$$

where  $F_{max}$  is the maximum compressive load of the testing machine, N;  $W$  is the thickness of the test piece, mm; and  $S = 4H$  is the span of the test piece, mm.

The formula for calculating the three-point bending tensile strength of pre-fracture shale specimens after processing is as follows [19]:

$$\sigma = \frac{3F_{max}S}{2W(H-a)^2} \quad (5)$$

where  $\sigma$  is the interface tensile stress, MPa.

$$K_{\sigma} = \frac{d\sigma}{du} \quad (6)$$

where  $d\sigma$  is the variation in interfacial tensile stress, MPa; and  $du$  is the variation in interfacial tensile displacement, mm.

Utilizing the DIC system, the horizontal displacement field of the shale specimen's natural weak interface was measured. Two reference calculation points, A and B, were selected on either side of the prefabricated fracture tip, perpendicular to the loading direction. The DIC image processing system provided the distance between these points for each state. Let  $k = 1$  represent the first photograph recorded by the CCD camera, with  $d_1$  being the initial distance between points A and B. At the  $k$ -th photograph, the reference point distance is  $d_k$ , where  $k$  is the CCD shooting sequence. Experimental testing and calculation models yielded the shale's mechanical parameters, as shown in Table 2, providing genuine and effective data support for subsequent numerical simulations of hydraulic fracture propagation in fissile shales.

**Table 2.** Results of the calculation of mechanical parameters for natural outcrop shale.

NF Dip	Specimen No.	Pmax (KN)	$\sigma_{\max}$ (MPa)	$K_{IC}$ (MPa/m <sup>1/2</sup> )	$K\sigma$ (GPa/m)
30°	S30-1	1.23	4.88	0.325	52.8
	S30-2	0.62	2.29	0.266	41.2
	S30-3	1.14	4.27	0.317	51.6
	S30-4	1.06	3.51	0.308	50.1
60°	S60-1	1.25	5.02	0.328	53.2
	S60-2	1.35	5.24	0.332	53.7
	S60-3	1.50	5.45	0.341	54.6
	S60-4	1.57	5.84	0.345	54.9
90°	S90-1	1.15	4.31	0.317	51.6
	S90-2	1.17	4.39	0.319	51.9
	S90-3	1.18	4.43	0.319	51.9
	S90-4	1.20	4.68	0.322	52.5

### 3. Mathematical Physics Equations

#### 3.1. Cohesive Unit Damage Model

The initiation and propagation of fractures are described using CZM elements with bilinear T-delta constitutive relationships (Figure 5). This approach not only avoids the issue of stress singularity at the fracture tip in traditional fracture mechanics but also integrates into the finite element computational framework, ensuring accuracy while reducing computational costs. In the figure,  $\bar{T}$  is stress obtained by the current strain according to the stiffness before damage;  $T_{\max}$  is maximum stress the unit can withstand before damage;  $T_a$  is actual stress on the element;  $\delta_f$ ,  $\delta_{\max}$ , and  $\delta_0$  are the displacement when the element is completely destroyed, the maximum displacement reached during loading, and the displacement at initial damage, respectively; and  $D$  is damage factor.

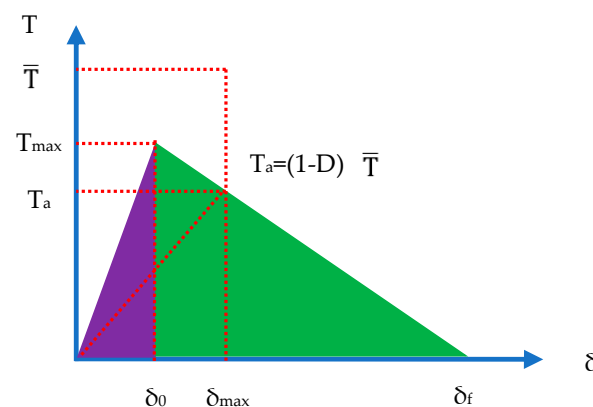


**Figure 5.** Cohesive unit damage T-delta criterion.

The initial damage of the cohesive unit is judged based on the quadratic nominal stress criterion:

$$\left(\frac{\langle t_n \rangle}{t_n^0}\right)^2 + \left(\frac{t_s}{t_s^0}\right)^2 + \left(\frac{t_t}{t_t^0}\right)^2 = 1 \quad (7)$$

where  $t_n$ ,  $t_s$ , and  $t_t$  are the current stresses in the normal direction, the first tangential direction, and the second tangential direction of the cohesive element, respectively, Pa;  $t_n^0$ ,  $t_s^0$ , and  $t_t^0$  are the normal, first tangential, and second tangential critical stresses of the cohesive element, namely the tensile and shear strength of the rock, Pa; symbol  $\langle \rangle$  is a cohesive unit that is only tensile but not compressive.

The damage evolution model of cohesive unit is:

$$\begin{cases} t_n = (1 - D)\bar{t}_n \\ t_s = (1 - D)\bar{t}_s \\ t_t = (1 - D)\bar{t}_t \end{cases} \quad (8)$$

where  $\bar{t}_n$ ,  $\bar{t}_s$ , and  $\bar{t}_t$  are the stresses calculated in the three directions of the cohesive unit according to the linear elastic deformation in the undamaged stage.

When fractures initiate and propagate, satisfying the conditions for damage, the adoption of the BK energy criterion comes into play, namely:

$$\begin{aligned} G_n^C + (G_s^C - G_n^C) \left\{ \frac{G_s^C}{G_T^C} \right\} &= G^C \\ G_T &= G_n + G_s \end{aligned} \quad (9)$$

where  $G_n^C$ , and  $G_s^C$  represent the critical fracture energy release rates required for fracture unit failure, measured in N/m.  $G_n$ ,  $G_s$  represent the normal and shear fracture energy release rates, measured in N/m.  $\eta$  denotes the material parameter.

### 3.2. Fluid Flow within Fractures

The fluid in the cohesive cell flows in the normal direction (perpendicular to the upper and lower surfaces) and tangentially, as in Figure 6.

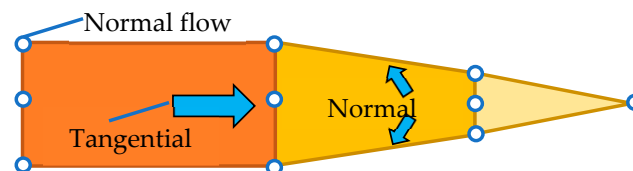


**Figure 6.** Cohesive unit fluid flow diagram.

Assuming that the fluid inside the fracture is an incompressible Newtonian fluid, the fluid flow inside the fracture is approximated as a parallel plate flow, and its tangential flow is calculated as:

$$q_f = -\frac{\omega^3}{12\mu} \nabla p_f \quad (10)$$

where  $q_f$  is tangential flow,  $\text{m}^3/\text{s}$ ;  $\nabla p_f$  is pressure gradient in the length of the cohesive cell, Pa/m;  $\omega$  is fracture width, m; and  $\mu$  is fracturing fluid viscosity, Pa·s.

The fluid leakage into the formation within the fracture is:

$$\begin{cases} q_t = c_t(p_f - p_t) \\ q_b = c_b(p_f - p_b) \end{cases} \quad (11)$$

where  $q_f$ , and  $q_b$  are the normal volumetric flow rates of the upper and lower surfaces, respectively,  $\text{m}^3/\text{s}$ ;  $c_f$ , and  $c_b$  are the filtration coefficients of the upper and lower surfaces,



respectively,  $\text{m}^3/(\text{Pa}\cdot\text{s})$ ; and  $p_t$ ,  $p_b$ , and  $p_f$  are the pore pressure at the upper and lower surfaces of the fracture and the fluid pressure in the cohesive unit, respectively, Pa.

The fluid within the fracture satisfies the principle of mass conservation, described by the equation.

$$\frac{\partial w}{\partial t} \nabla [q + (q_t + q_b)] = Q(t)\delta(x, y) \quad (12)$$

where  $q$  is the fluid flow rate within the fracture,  $\text{m}^3/\text{s}$ .

### 3.3. Interaction Settings between HF and NF

The nonlinear equation solver ABAQUS is employed to solve the aforementioned equations. The deformation of the rock matrix and the fluid seepage equations are integrated into the C3D8P element, resulting in 3 displacement nodes and 8 seepage nodes. The equations for fracture initiation and propagation are coupled with the CZM element COH3D8P. Furthermore, by utilizing the Merge command in the solver's mesh module, the nodes of the elements at the interaction zone between hydraulic fractures and natural fractures are merged into a common pore pressure node, ensuring free fluid pressure transmission within the hydraulic and natural fractures, as shown in Figure 7.

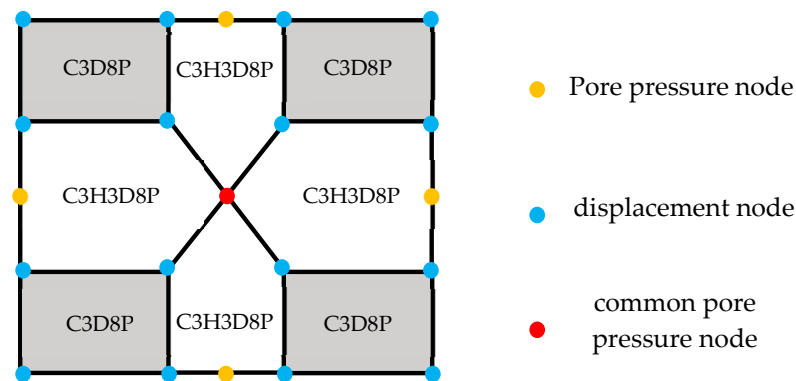


**Figure 7.** Schematic diagram of merging nodes at the intersection of hydraulic fractures and hydraulic fracture units.

### 3.4. Wellbore Fluid Flow Equation

After injecting the fracturing fluid to the bottom of the well, the total injection rate is distributed throughout the wellbore-fracture system according to the flow law, much like the flow of current in an electrical circuit. The total injection volume equals the sum of the flow rates in each branch fracture.

$$Q_{total} = \sum_i^n Q_i, i = 1, 2, 3, \dots, n \quad (13)$$

where  $Q_{total}$  is total flow of the wellbore,  $\text{m}^3/\text{min}$ ; and  $Q_i$  is flow rate of a cluster of fractures,  $\text{m}^3/\text{min}$ .

The effective fluid model inside a horizontal wellbore should consider the following characteristics: 1. frictional pressure loss along the wellbore; 2. perforation frictional loss; 3. proppant erosion of the perforation. The coupled model between the horizontal wellbore and the formation is shown in Figure 8, where the wellhead pressure is indicated:

$$P_t = P_{fra} + P_{pf} + P_{wellbore} - P_h \quad (14)$$

where  $P_t$  is surface wellhead pressure, Pa;  $P_{fra}$  is fracture opening pressure, Pa;  $P_h$  is wellbore hydrostatic column pressure, Pa;  $P_{pf}$  and  $P_{wellbore}$  are the perforation friction and the fracturing fluid friction along the wellbore, respectively, Pa. Since the model focuses

on the fracture propagation in the horizontal wellbore, the wellbore hydrostatic column pressure is zero.

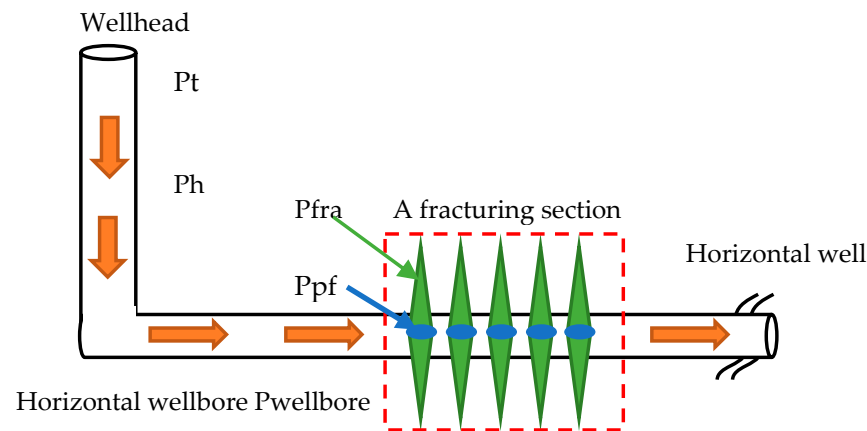


**Figure 8.** Wellbore-formation coupling model.

### 3.4.1. Perforation Friction

Each cluster of fractures is in a “parallel” state, where the liquid influx is controlled by the perforation resistance, roughness resistance, and internal flow resistance of the fracture. Both roughness resistance and perforation resistance are near-well resistances with similar flow-limiting mechanisms, thus the roughness resistance can be considered equivalent to the perforation resistance, as mentioned in [20]:

$$\Delta P_{pf} = \frac{0.2369\rho}{D_p^4 C_d^2} \left( \frac{Q_i}{N} \right)^2 \quad (15)$$

where  $Q_i$  is the flow rate of fracturing fluid entering the  $i$ -th fracture,  $\text{m}^3/\text{s}$ ;  $D_p$  is the diameter of the perforation hole,  $\text{m}$ ; and  $\rho$  is fracturing fluid density,  $\text{kg}/\text{m}^3$ .

Among them, the flow coefficient can be defined as the ratio of the flow channel area to the flow channel diameter:

$$C_d = \left( \frac{Q}{Q_i} \right) = C_c C_v = \frac{D_1}{d} \quad (16)$$

where  $C_d$  is the discharge coefficient at the hole inlet,  $\text{Pa}$ ;  $N$  is the number of holes in the cluster.

### 3.4.2. Wellbore Flow Friction

The flow of fracturing fluid in the wellbore is a circular pipe flow, and the Darcy–Weisbach pipe flow friction is used to calculate [21]:

$$\begin{cases} \Delta P_f = (C_L + K_i) \frac{\rho V^2}{2} \\ C_L = \frac{fL}{D_h} \end{cases} \quad (17)$$

where  $C_L$  is along-travel friction loss factor;  $K_i$  is directional loss factor;  $f$  is the coefficient of friction of the inner wall of the column;  $V$  is pipeline flow rate,  $\text{m}/\text{s}$ ;  $L$  is fracturing string length,  $\text{m}$ ; and  $D_h$  is the hydraulic diameter,  $\text{m}$ .

The friction loss coefficient along the way is affected by the Reynolds number and the inner wall roughness of the pipe string, and is calculated using the Churchill full-flow model:

$$\begin{cases} f = 8 \left[ \left( \frac{8}{Re} \right)^{12} + \frac{1}{(A+B)^{1.5}} \right]^{\frac{1}{12}} \\ A = \left[ -2.457 \ln \left( \left( \frac{7}{Re} \right)^{0.9} + 0.27 \left( \frac{K_s}{D_h} \right) \right) \right]^{16} \\ B = \left( \frac{37350}{Re} \right)^{16} \end{cases} \quad (18)$$

where  $Re$  is the Reynolds number, dimensionless; and  $K_s$  is the roughness of the fracturing pipeline.

#### 4. Numerical Model

##### 4.1. Three-Dimensional Finite Element Model

Figure 9 illustrates the three-dimensional finite element model designed for a reservoir containing natural fractures and multiple hydraulic fractures. The axes  $x$ ,  $y$ , and  $z$  represent the directions of minimum horizontal principal stress, maximum horizontal principal stress, and vertical stress, respectively. The dimensions along the  $x$  and  $z$  directions are both 15 m, while the fracture length along the  $y$  direction is 30 m. Within this model, two natural fractures (referred to as NF1-2) are horizontally embedded along the  $x$  direction, and three hydraulic fractures (referred to as HF1-3) are vertically inserted along the  $z$  direction to simulate the initiation and propagation of hydraulic fractures. This comprehensive model consists of distinct regions: two interlayers at the top and bottom, and a central reservoir. The red region represents the path of hydraulic fracture propagation within the reservoir, the blue region signifies the path of hydraulic fracture propagation within the interlayers, and the green region signifies the presence of natural weak interfaces. The intersection angle ( $\theta$ ) between hydraulic fractures and natural fractures, as well as the dip angle ( $\beta$ ) between natural fractures and the horizontal plane, have been meticulously considered. The perforation clusters, horizontal wellbore, and injection points within the reservoir are bound together through the compilation of an INP file. By continuously injecting fracturing fluid into the reservoir through wellbore elements, multiple clusters of fractures initiate and propagate simultaneously, enabling sensitivity analysis of various parameters during the fracturing process. The fundamental parameters of the model are derived from well logging interpretations in a specific fracturing segment of the X horizontal well in the southwestern region, as detailed in Table 3.

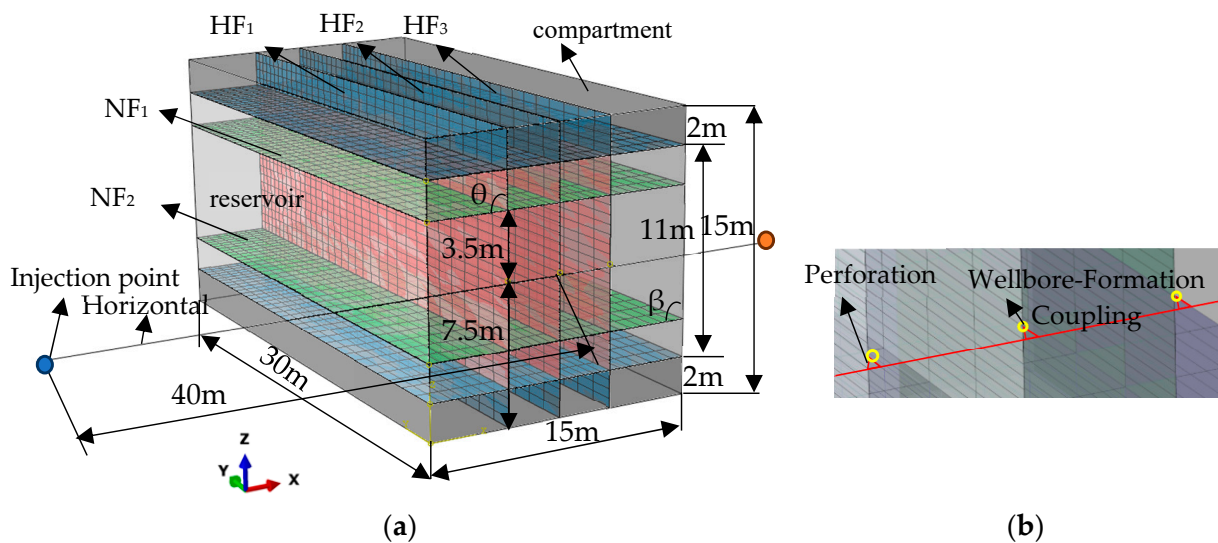


**Figure 9.** Numerical model of shale reservoir. (a) A three-dimensional finite element model of multi fracture propagation in a reservoir with natural fractures; (b) coupling treatment method of wellbore formation.

**Table 3.** Basic parameters of the model.

Formation Parameters	Value	Construction Parameters	Value
Young's modulus/GPa	39	Initial pore Pressure/MPa	50
Poisson's ratio	0.23	Injection rate/ $\text{m}^3 \cdot \text{s}^{-1}$	0.01
In situ stress/MPa	74.7/79.6/86.8	Fracturing Fluid Viscosity/mPa·s	5
Permeability coefficient/ $\text{m} \times \text{s}^{-1}$	$1.5 \times 10^{-8}$	Clusters	3
Filter loss coefficient/ $\text{m} \times \text{Pas}^{-1}$ (HF/NF)/( $\text{m} \cdot (\text{Pas}^{-1})$ )	$1 \times 10^{-13}/1 \times 10^{-14}$	Cluster spacing/m	2.5
tensile strength (HF/NF)/MPa	8/3	Perforation density combination	20-20-20
Shear strength (HF/NF)/MPa	20/12	Perforation hole diameter/m	0.015

#### 4.2. Model Validation

For the investigation of the multi-cluster fracture propagation in naturally fractured shale reservoirs, the simulation parameters used in Liu's study are adopted [22]. When the approximation angle is  $90^\circ$ , the natural fractures have an inclination angle of  $0^\circ$ , and the inter-cluster spacing is set to 2 m and 3 m, the expansion behavior of multiple fractures intersecting with natural fractures is examined, as shown in Figure 10. Let HF1, HF2, and HF3 represent the hydraulic fractures along the positive x-axis. From the figure, it can be observed that the hydraulic fractures induce shear sliding along the natural fracture surfaces, with the fractures on both sides penetrating the natural fractures. The interference of stress between multiple clusters of hydraulic fractures causes difficulties for the HF2 cluster to accept fluid injection, resulting in diversion by the natural fractures. The simulated results presented in Table 4 are in good agreement, with a simulation error ranging from 2.04% to 3.15%. Hence, this validates the model's ability to accurately simulate the expansion of multi-cluster fractures in naturally fractured shale reservoirs.

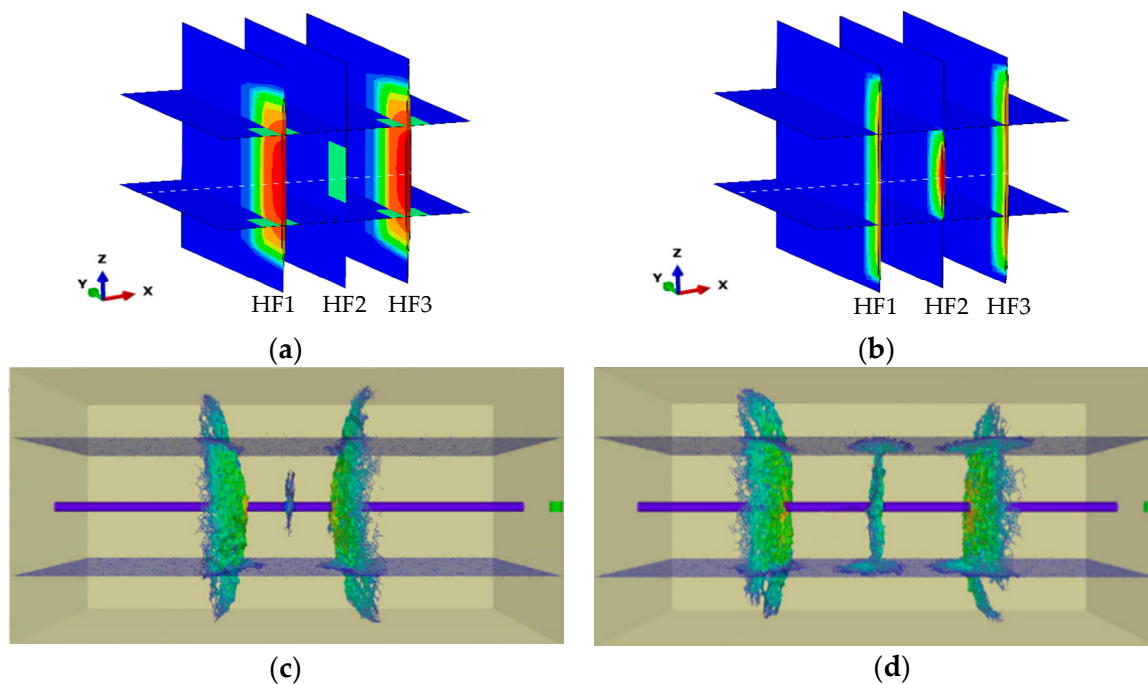


**Figure 10.** Numerical model of shale reservoir: (a) Cluster spacing of this model is 2 m; (b) cluster spacing of this model is 3 m; (c) cluster spacing of Liu model is 2 m; (d) cluster spacing of Liu model is 3 m.

**Table 4.** Comparison of seam height calculation results between this model and the Guo model in literature.

Results	Approach Angle	Cluster Spacing	Interaction between HF and NF	Expansion Height (HF1–HF3)	Simulation Error
this model Liu model	90°	2 m	HF1 and HF2 are penetrated HF3 is an invalid fracture	9.5 m, 0 m, 9.5 m 9.2 m, 0.5 m, 9.3 m	3.15%
this model Liu model	90°	3 m	HF1 and HF2 are penetrated HF3 is intercepted and diverted	9.6 m, 4.8 m, 9.6 m 9.8 m, 4.6 m, 9.7 m	2.04%

As mentioned earlier, numerous scholars have conducted extensive true triaxial hydraulic fracturing laboratory experiments to investigate the actual propagation patterns of hydraulic fractures interacting with natural fractures and analyze their interactions [23]. The summarized and compared results of these laboratory experiments are depicted in Figure 11. The comparative analysis reveals a high degree of agreement between the numerical simulation results and the experimental findings, thereby further validating the effectiveness and accuracy of the finite element method in simulating the intersection of multiple fractures.

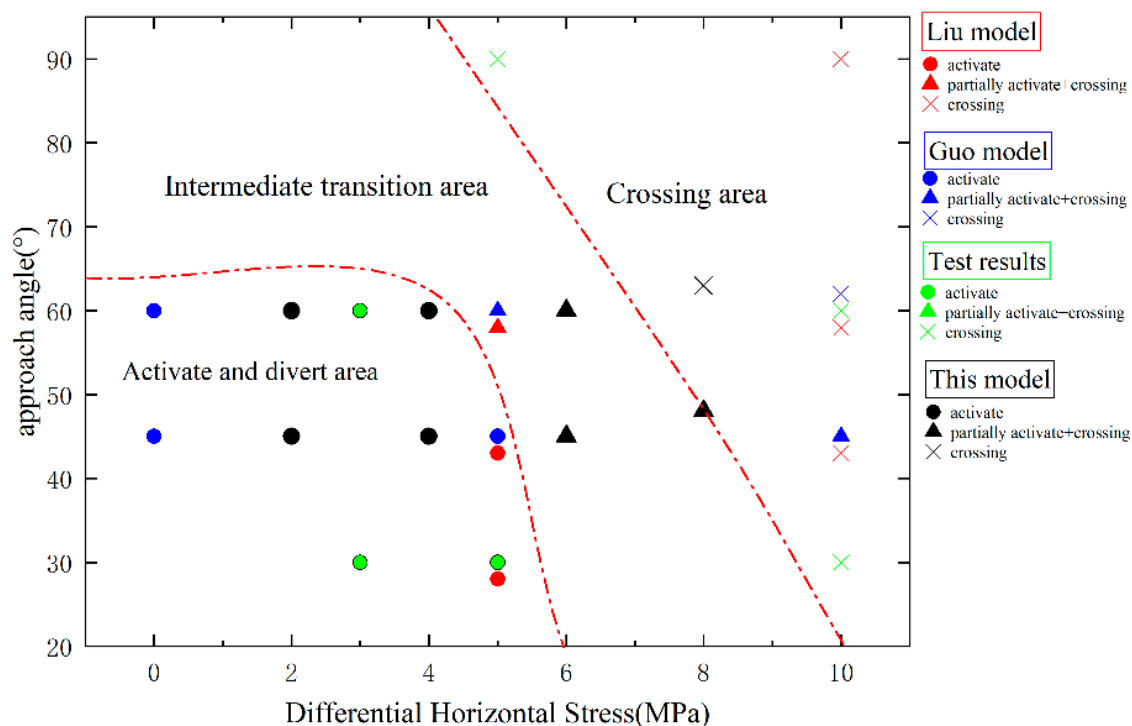


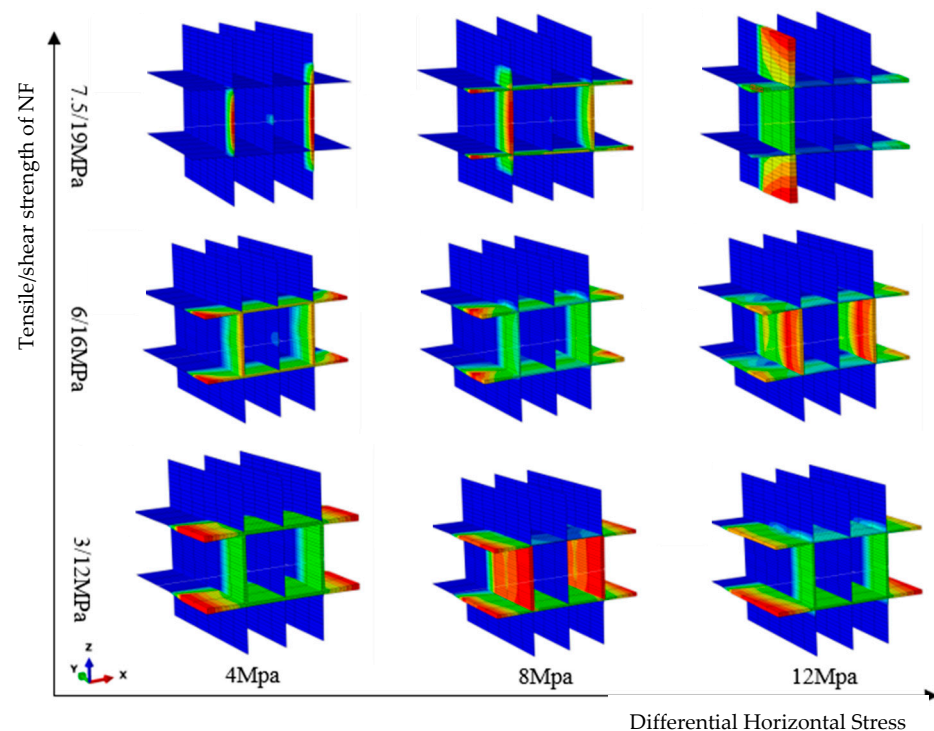
**Figure 11.** Comparison of multiple model calculation results with experimental results.

## 5. Results

We investigated the influence of construction parameters and natural fracture cementation strength on the interaction between hydraulic fractures (HFs) and natural fractures (NFs) when the NFs were horizontally embedded orthogonally with a tilt angle of 0°. Specifically, we examined the expansion patterns of hydraulic fractures under different horizontal stress differentials of 4 MPa, 8 MPa, and 12 MPa, while keeping the vertical stress and minimum horizontal principal stress constant. We explored the expansion characteristics of hydraulic fractures under various engineering variables, while maintaining the remaining model parameters consistent with those presented in Table 3.

### 5.1. NF Bond Strength

Different cementation strengths (tensile/shear) of natural fractures were simulated, namely 3/12, 6/16, and 7.5/19 MPa, as depicted in Figure 12. In the figure, for a smaller horizontal stress differential (4 MPa) and weaker cementation strength of NFs (3/16 MPa), the HF is more prone to initiate shear failure in NFs, resulting in longer extension and a larger network of interconnected fractures. Conversely, when the cementation strength of NFs approximates the strength of the rock matrix (7.5/19 MPa), the HF exhibits greater propensity to penetrate NFs and expand in the vertical fracture height direction. For a larger horizontal stress differential (12 MPa), lower cementation strength of NFs corresponds to a longer activation length of HF in NFs and a larger area of hydraulic fracturing stimulation.



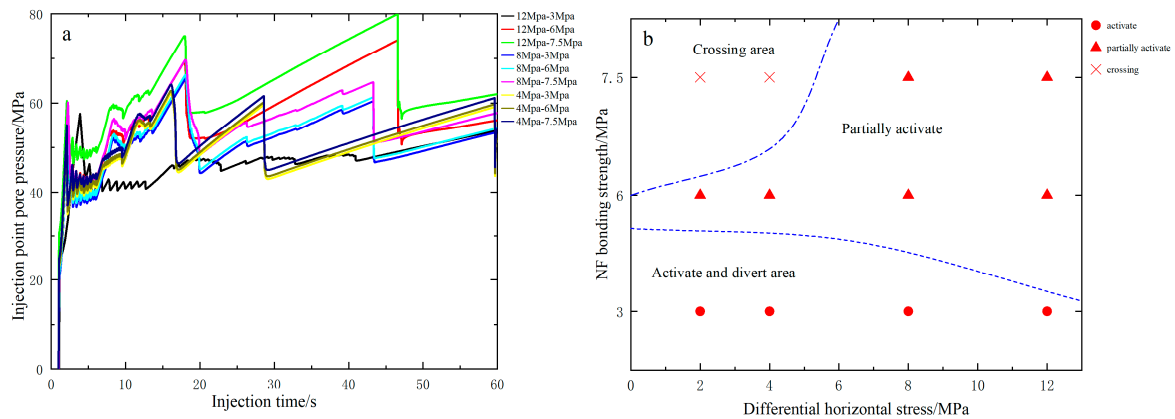
**Figure 12.** Pattern of HF propagation under different NF bonding strengths.

Figure 13 illustrates the results of HF injection point pressure and propagation modes with NF cementation strength as a variable. In Figure 13a, as the cementation strength of NFs increases, the rock fracturing pressure and wellbore pressure also increase, with a peak pressure of 12–7.5 MPa. In Figure 13b, for low cementation strength (3/12 MPa), a larger horizontal stress differential facilitates the opening of HF in NFs. Conversely, for high cementation strength (7.5/19 MPa), a smaller horizontal stress differential allows HF to more easily penetrate NFs. When the cementation strength is equal, a larger horizontal stress differential leads to increased fracture width and a greater likelihood of shear failure in NFs. Only when the cementation strength of NFs is lower than that of the rock matrix can the natural fracture surface potentially be opened, thereby enabling the formation of a complex fracture network.

### 5.2. Perforation Density

The simulation results for different perforation density combinations, namely 10-10-10, 10-20-10, and 20-20-20, are shown in Figure 14. In the figure, for a smaller perforation density (10-10-10), the frictional resistance of the perforation hole increases, resulting in higher initiation pressure for HF. The frictional resistance between the perforation holes partially mitigates the stress interference between clusters, allowing all three clusters to develop and expand. In the case of non-uniform perforation (10-20-10), the frictional resistance

of the intermediate cluster effectively alleviates the stress interference between clusters, leading to uniform development of fractures in each cluster. Moreover, a larger horizontal stress differential results in longer HF propagation along the maximum principal stress fracture, forming a larger complex fracture network. Conversely, for higher perforation density (20-20-20), the frictional resistance of the perforation holes decreases, leading to lower initiation pressure for HF. The two side clusters develop symmetrically along the NF interface, while the middle cluster encounters obstruction in its expansion, rendering it an ineffective perforation cluster.



**Figure 13.** Calculation results under different NF bonding strengths: (a) injection point pore pressure; (b) fracture propagation mode.

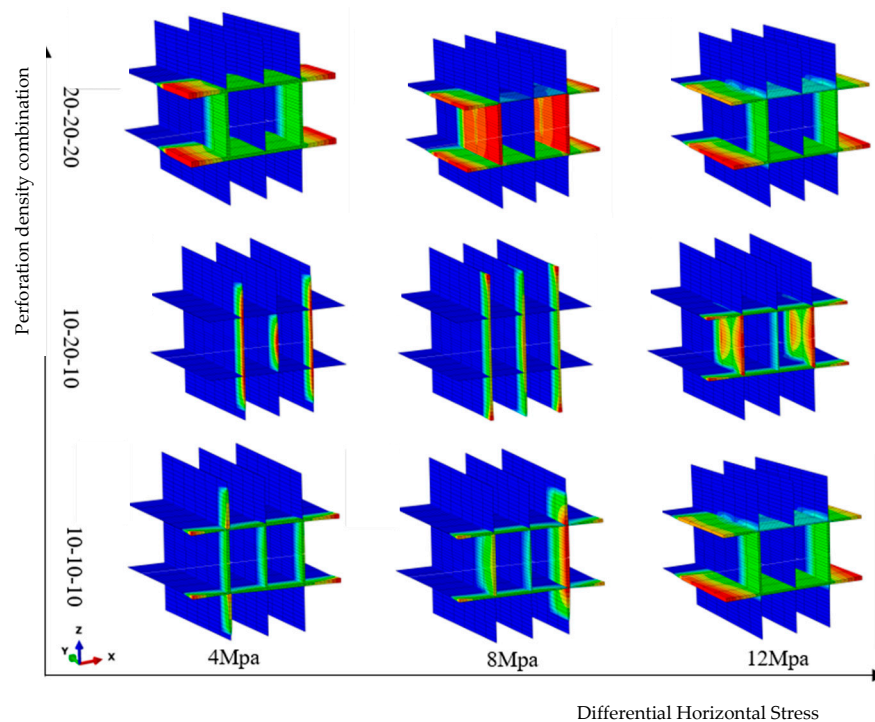


**Figure 14.** Pattern of HF propagation under different perforation density combination.

Figure 15 illustrates the results of HF injection point pressure and propagation modes with perforation density as a variable. In Figure 15a, for a uniformly distributed and lower density of perforation holes (10-10-10), it can be deduced from Equation (10) that the perforation frictional resistance is inversely correlated with the number of perforation holes. Thus, with a smaller density, the frictional resistance of the perforation holes increases, resulting in higher pressure required for HF extension and larger injection point pressure

at the wellhead. Notably, when the stress differential is 4 MPa, it corresponds to the peak injection point pressure. In Figure 15b, as the perforation hole density increases, the perforation frictional resistance decreases, making it easier for HF to propagate and open the natural fracture surface.

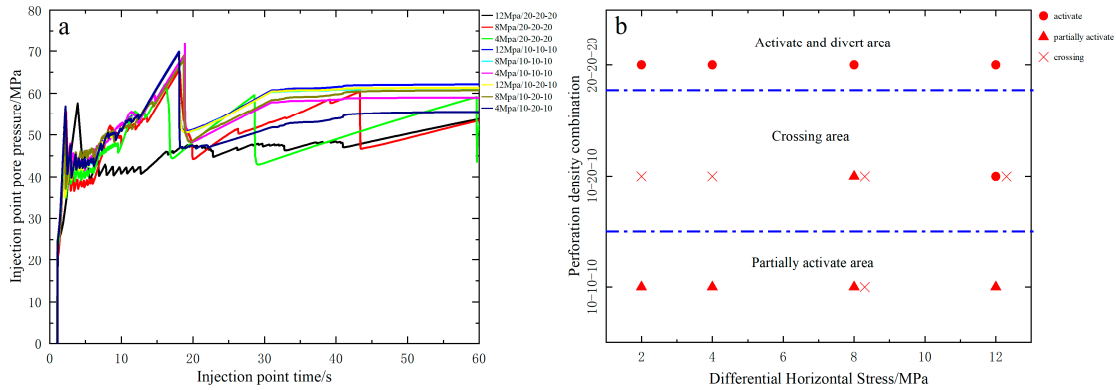


**Figure 15.** Calculation results under different perforation densities: (a) injection point pore pressure; (b) fracture propagation mode.

### 5.3. Injection Rate

Simulations were conducted with different injection rates of  $0.001 \text{ m}^3/\text{s}$ ,  $0.005 \text{ m}^3/\text{s}$ , and  $0.01 \text{ m}^3/\text{s}$ , and the results are presented in Figure 16. In the figure, for the lower injection rate ( $0.001 \text{ m}^3/\text{s}$ ), a larger horizontal stress differential leads to increased lengths of HF propagation along the maximum principal stress fracture and shear displacement along the natural interface. Conversely, for the higher injection rate ( $0.01 \text{ m}^3/\text{s}$ ), the filtration loss of the fracturing fluid is significantly reduced. This results in the confinement pressure initiating HF propagation and redirecting it along the natural fracture surface. Consequently, the affected zone of HF widens, leading to a substantial increase in the volume of reservoir modification. However, it should be noted that the injection rate of the fracturing fluid only affects the morphology of the fracture propagation and does not effectively balance the interference of stress between clusters. Consequently, the hindered inflow of fluid into the intermediate cluster results in ineffective perforation clusters.

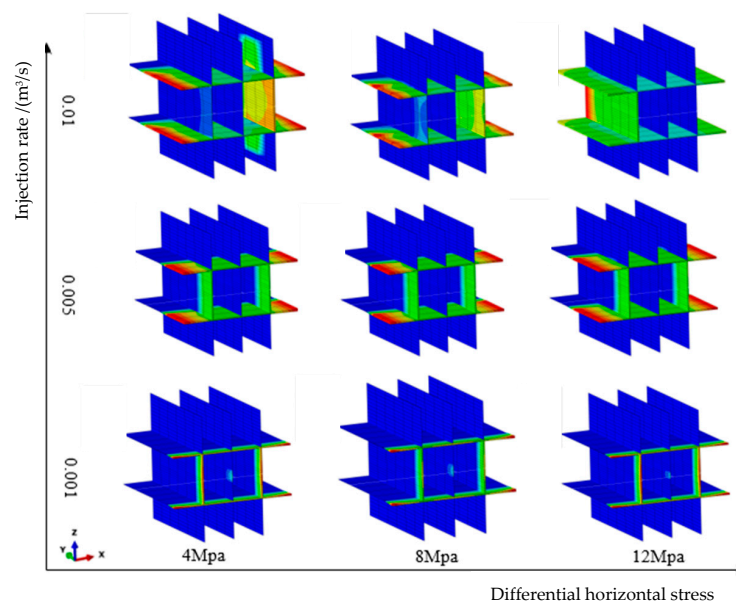


**Figure 16.** Pattern of HF propagation under different injection rates.



Figure 17 illustrates the results of HF injection point pressure and propagation modes with injection rate as a variable. In Figure 17a, as the injection rate increases, the pressure at the wellhead also increases, with 12 MPa and 0.01 m<sup>3</sup>/s representing the peak injection point pressure. In Figure 17b, with the augmentation of the injection rate, the flow rate increases as well. This leads to an expansion in the affected zone of HF, resulting in longer and wider fractures. Consequently, the likelihood of NFs experiencing shear failure and the formation of a complex network of fractures is heightened. Therefore, by enhancing the injection rate, an increased occurrence of shear failure in NFs can be observed, leading to a greater area of interconnected NFs and the formation of a more intricate fracture network.

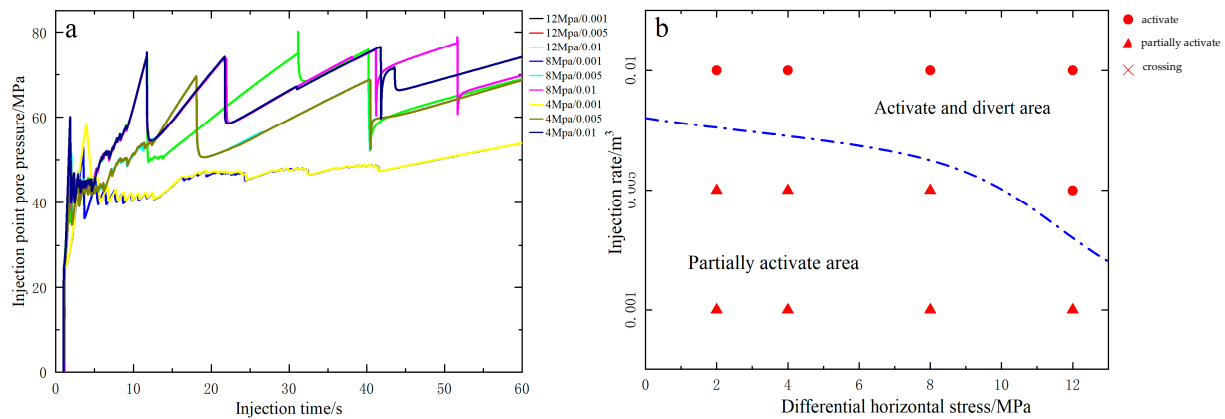


**Figure 17.** Calculation results under different injection rates: (a) injection point pore pressure; (b) fracture propagation mode.

#### 5.4. Fracturing Fluid Viscosity

In Figure 18, different fracturing fluid viscosities are simulated, namely 1 mPa·s, 5 mPa·s, and 10 mPa·s. As depicted in the figure, with an increase in the viscosity of the fracturing fluid, the filtration loss of the fluid decreases while the flow resistance of the fluid increases. This results in an expansion of the fracture width, leading to a greater occurrence of shear failure in more natural fractures (NFs). The affected zone of hydraulic fracturing (HF) widens, but its length decreases. Consequently, the area of NFs alteration initially increases and then gradually decreases. Under the same fracturing fluid viscosity, a higher difference in horizontal stress leads to longer HF fractures along the maximum principal stress and greater shear displacement along the natural interface. However, the rate of fluid injection during hydraulic fracturing only affects the expansion morphology of the fractures and cannot balance the interference of stress between clusters, causing blockage of fluid inflow in the intermediate clusters and rendering them ineffective.

Figure 19 illustrates the results of HF injection point pressure and propagation modes with fracturing fluid viscosity as a variable. In Figure 19a, the variation in fracturing fluid viscosity has a minimal impact on the injection point pressure. However, at a viscosity of 1 mPa·s and an injection point pressure of 4 MPa, there exists a minimum peak where the connectivity area of natural fractures (NFs) is at its smallest. This reduces the likelihood of shear failure occurring on the natural fracture surfaces. In Figure 19b, under high fracturing fluid viscosity, the flow resistance within the wellbore increases, resulting in higher bottomhole pressures that facilitate the opening and diversion of HF towards NFs. When the fracturing fluid viscosity remains constant, the difference in horizontal stress becomes the dominant factor in HF propagation. The greater the difference in stress, the larger the area of NFs alteration becomes. Therefore, it is essential to establish an appropriate range of fracturing fluid viscosity based on reservoir characteristics to facilitate the formation of a complex fracture network.

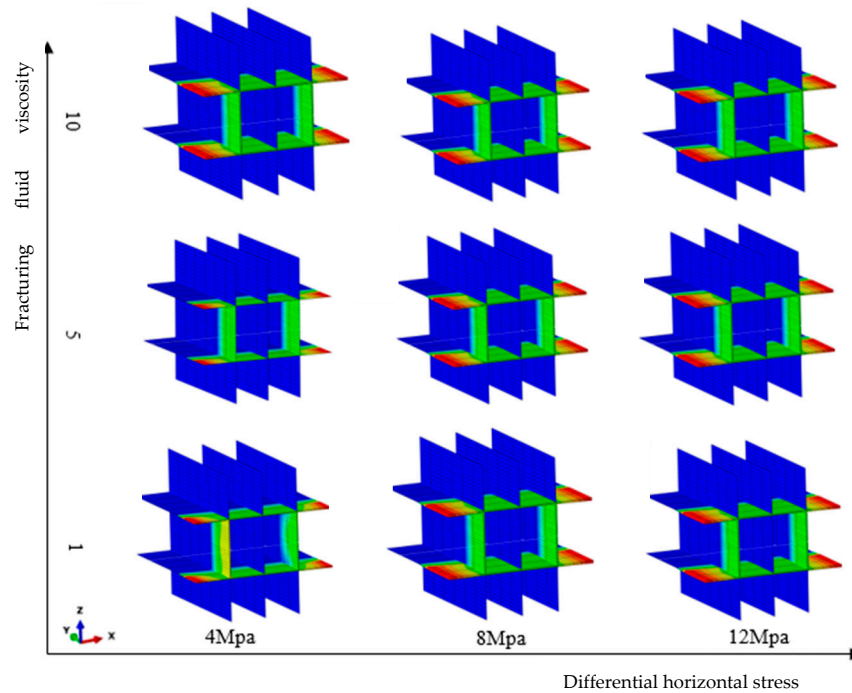


Figure 18. Pattern of HF propagation under different viscosities of fracturing fluids.

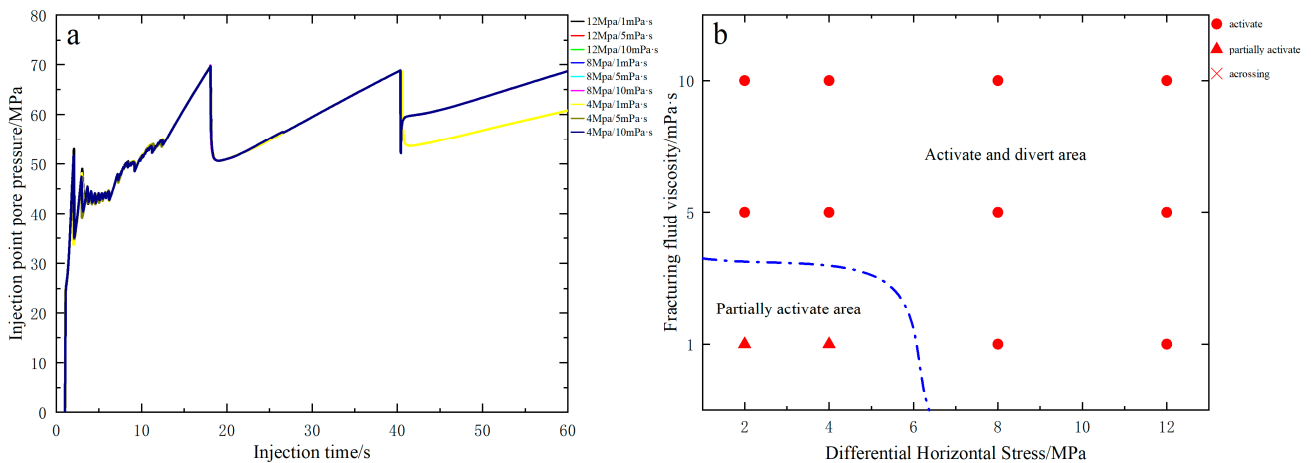


Figure 19. Calculation results under different viscosities of fracturing fluids: (a) injection point pore pressure; (b) fracture propagation mode.

### 6. Conclusions

In this study, we employed indoor TPB experiments in conjunction with DIC technology to measure the mechanical characteristic parameters of natural shale cores. Utilizing the coupled stress-permeability-damage zone method (CZM), we established a three-dimensional model that accounts for the competition and expansion of multiple hydraulic fractures in horizontal wells, considering the presence of natural fractures. Through this model, we investigated the interaction mechanisms between hydraulic fractures and natural weak planes, providing a quantitative representation of the expansion behavior of hydraulic fractures under the influence of geological and engineering parameters. The specific conclusions are as follows:

- (1) Reservoir stress difference is a key parameter that influences the interactive expansion pattern of hydraulic fractures (HFs) and natural fractures (NFs). The magnitude of horizontal principal stress dominates the formation mode and geometric shape of complex fracture networks. Greater stress difference leads to a stronger ability of HFs

to open natural fracture surfaces and a more pronounced shear-sliding along the weak interfaces. Conversely, HFs will propagate through the natural fracture surfaces in the direction of fracture height when the stress difference is smaller.

- (2) Only when the cohesive strength of NFs is lower than the strength of the rock matrix can NF interfaces be initiated. Higher cohesive strength results in HFs showing no significant passivation phenomenon on natural fracture surfaces and enhances their ability to penetrate through the natural fracture surfaces. On the other hand, lower cohesive strength makes HFs more prone to passivation, leading to shear failure of NFs. Consequently, HFs open up and redirect along NFs for further expansion.
- (3) The combination of perforation density is a significant factor contributing to inter-cluster stress interference. A higher density of boreholes and a larger number of clusters result in an increased stress shadow area. Consequently, the ability of fluid penetration within the shadow region of perforation clusters weakens, leading to the ineffectiveness of intermediate cluster HF2 in forming fractures. When the perforation frictional resistance reaches a certain threshold, the dynamic allocation of fluid flow among multiple fractures shifts from being governed by inter-cluster shadows to the magnitude of perforation frictional resistance. Strategically arranging a lower pore density and fewer boreholes effectively increases pore resistance, alleviates inter-cluster stress interference, and promotes the balanced development of multiple fractures.
- (4) Increasing the injection rate and viscosity of the fracturing fluid facilitates the propagation of all perforation clusters within the fractures, thereby enhancing the likelihood of opening natural fractures (NFs). As the injection rate and fracturing fluid viscosity increase, there is a notable increase in shear displacement along the natural fracture surfaces, which promotes the development of complex fractures in reservoirs. However, both factors have a threshold beyond which they fail to effectively improve reservoir stimulation.

**Author Contributions:** Writing—review & editing, Q.C.; Conceptualization, Z.H.; Writing—review & editing, X.L.; Formal analysis, P.X.; Methodology, L.T.; Project administration, W.L.; Investigation, J.X.; Supervision, M.W.; Validation, Y.C.; Visualization, L.L. All authors have read and agreed to the published version of the manuscript.

**Funding:** Supported by the Sinopec Science and Technology Department project “Key Technologies for Volume Fracturing of Shallow and Medium Tight Sandstone Gas Reservoirs in Western Sichuan” (P22047).

**Institutional Review Board Statement:** Not applicable.

**Informed Consent Statement:** Not applicable.

**Data Availability Statement:** Not applicable.

**Conflicts of Interest:** The authors declare no conflict of interest.

## References

1. Zou, C.N.; Dong, D.Z.; Wang, S.J.; Li, J.Z.; Li, X.J.; Wang, Y.M.; Li, D.H.; Cheng, K.M. Formation mechanism, geological characteristics and resource potential of Shale gas in China. *Pet. Explor. Dev.* **2010**, *37*, 641–653. [[CrossRef](#)]
2. Zou, C.N.; Pan, S.Q.; Jing, Z.H.; Gao, J.L.; Yang, Z.; Wu, S.T.; Zhao, Q. Shale oil and gas revolution and its impact. *Acta Pet. Sin.* **2020**, *41*, 1.
3. Zou, C.N.; Zhu, R.K.; Dong, D.Z.; Wu, S.T. Scientific and technological progress, development strategy and policy suggestion regarding shale oil and gas. *Acta Pet. Sin.* **2022**, *43*, 1675–1686.
4. Chen, Z.; Bunger, A.; Zhang, X.; Jeffrey, R.G. Cohesive zone finite element-based modeling of hydraulic fractures. *Acta Mech. Solida Sin.* **2009**, *22*, 443–452. [[CrossRef](#)]
5. Wang, W.; Zhang, K.; Su, Y.; Tang, M.; Zhang, Q.; Sheng, G. Fracture Network Mapping Using Integrated Micro-Seismic Events Inverse with Rate-Transient Analysis. In Proceedings of the 11th International Petroleum Technology Conference, Beijing, China, 26–28 March 2019.
6. Warpinski, N.R.; Teufel, L.W. Influence of Geologic Discontinuities on Hydraulic Fracture Propagation. *J. Pet. Technol.* **1987**, *39*, 209–220. [[CrossRef](#)]

7. Zhou, J.; Chen, M.; Jing, Y.; Zhang, G.Q. Experimental study on propagation mechanism of hydraulic fracture in naturally fractured reservoir. *Acta Pet. Sin.* **2007**, *28*, 109–113.
8. Blanton, T.L. An Experimental Study of Interaction between Hydraulically Induced and Pre-Existing Fractures. In Proceedings of the SPE Unconventional Gas Recovery Symposium, Pittsburgh, PA, USA, 16–18 May 1982; p. SPE-10847-MS.
9. Yushi, Z.; Shicheng, Z.; Tong, Z.; Xiang, Z.; Tiankui, G. Experimental Investigation into Hydraulic Fracture Network Propagation in Gas Shales Using CT Scanning Technology. *Rock Mech. Rock Eng.* **2016**, *49*, 33–45. [[CrossRef](#)]
10. Guo, J.; Zhao, X.; Zhu, H.; Zhang, X.; Pan, R. Numerical simulation of interaction of hydraulic fracture and natural fracture based on the cohesive zone finite element method. *J. Nat. Gas Sci. Engng.* **2015**, *25*, 180–188. [[CrossRef](#)]
11. Gonzalez-Chavez, M.; Dahi Taleghani, A.; Olson, J.E. A cohesive model for modeling hydraulic fractures in naturally fractured formations. In Proceedings of the SPE Hydraulic Fracturing Technology Conference, The Woodlands, TX, USA, 3–5 February 2015.
12. De Pater, C.J.; Beugelsdijk, L.J.L. Experiments and numerical simulation of hydraulic fracturing in naturally fractured rock, Alaska Rocks 2005. In Proceedings of the 40th U.S. Symposium on Rock Mechanics (USRMS), Anchorage, AK, USA, 25–29 June 2005; American Rock Mechanics Association: Anchorage, AK, USA, 2005.
13. Nagel, N.B.; Gil, I.; Sanchez-Nagel, M.; Damjanac, B. Simulating hydraulic fracturing in real fractured rock—overcoming the limits of pseudo-3D models. In Proceedings of the SPE Hydraulic Fracturing Technology Conference, The Woodlands, TX, USA, 24–26 January 2011; Society of Petroleum Engineers: The Woodlands, TX, USA, 2011.
14. Zou, Y.S.; Zhang, S.C.; Ma, X.F.; Zhou, T.; Zeng, B. Numerical investigation of hydraulic fracture network propagation in naturally fractured shale formations. *J. Struct. Geol.* **2016**, *84*, 1–13. [[CrossRef](#)]
15. Roussel, N.P.; Sharma, M.M. Optimizing Fracture Spacing and Sequencing in Horizontal-Well Fracturing. *SPE Prod. Oper.* **2011**, *26*, 173–184. [[CrossRef](#)]
16. Manchanda, R.; Sharma, M.M.; Holzhauser, S. Time-dependent fracture-interference effects in pad wells. *SPE Prod. Oper.* **2014**, *29*, 274–287. [[CrossRef](#)]
17. Wu, R.; Kresse, O.; Weng, X. Modeling of interaction of hydraulic fractures in complex fracture networks. In Proceedings of the SPE Hydraulic Fracturing Technology Conference, The Woodlands, TX, USA, 6 February 2012.
18. Anderson, T.L. *Fracture Mechanics: Fundamentals and Applications*; CRC Press: Boca Raton, FL, USA, 2017.
19. Miao, Y.; Wei, C.H.; Niu, L.L.; Li, S.H.; Yu, Y.J. Calculation for tensile strength and fracture toughness of granite with three kinds of grain sizes using three-point-bending test. *PLoS ONE* **2018**, *13*, 108413.
20. Wu, K.; Olson, J.E. Mechanisms of Simultaneous Hydraulic-Fracture Propagation From Multiple Perforation Clusters in Horizontal Wells. *SPE J.* **2016**, *21*, 1000–1008. [[CrossRef](#)]
21. El-Rabba, A.M.; Shah, S.N.; Lord, D.L. New Perforation Pressure-Loss Correlations for Limited-Entry Fracturing Treatments. *SPE Prod. Facil.* **1999**, *14*, 63–71. [[CrossRef](#)]
22. Liu, X.; Qu, Z.; Guo, T.; Sun, Y.; Wang, Z.; Bakhshi, E. Numerical simulation of non-planar fracture propagation in multi-cluster fracturing with natural fractures based on Lattice methods. *Eng. Fract. Mech.* **2019**, *220*, 106625. [[CrossRef](#)]
23. Zhou, J.; Chen, M.; Jin, Y.; Zhang, G.Q. Analysis of fracture propagation behavior and fracture geometry using a tri-axial fracturing system in naturally fractured reservoirs. *Int. J. Rock Mech. Min. Sci.* **2008**, *45*, 1143–1152. [[CrossRef](#)]

**Disclaimer/Publisher’s Note:** The statements, opinions and data contained in all publications are solely those of the individual author(s) and contributor(s) and not of MDPI and/or the editor(s). MDPI and/or the editor(s) disclaim responsibility for any injury to people or property resulting from any ideas, methods, instructions or products referred to in the content.